Pulsed photoemission induced plasma breakdown

Asif Iqbal[1,*] , Brian Z Bentz[2,*] , Yang Zhou[1] , Kevin Youngman[2] and Peng Zhang[1,*]

[1] Department of Electrical and Computer Engineering, Michigan State University, East Lansing, MI 48824-1226, United States of America
[2] Sandia National Laboratories, Albuquerque, NM 87123-3453, United States of America

E-mail: iqbalas3@msu.edu, bzbentz@sandia.gov and pz@egr.msu.edu

CrossMark

Abstract

This article characterises the effects of cathode photoemission leading to electrical discharges in an argon gas. We perform breakdown experiments under pulsed laser illumination of a flat cathode and observe Townsend to glow discharge transitions. The breakdown process is recorded by high-speed imaging, and time-dependent voltage and current across the electrode gap are measured for different reduced electric fields and laser intensities. We employ a 0D transient discharge model to interpret the experimental measurements. The fitted values of transferred photoelectron charge are compared with calculations from a quantum model of photoemission. The breakdown voltage is found to be lower with photoemission than without. When the applied voltage is insufficient for ion-induced secondary electron emission to sustain the plasma, laser driven photoemission can still create a breakdown where a sheath (i.e. a region near the electrode surfaces consisting of positive ions and neutrals) is formed. This photoemission induced plasma persists and decays on a much longer time scale ($\sim 10s$ μs) than the laser pulse length (30 ps). The effects of different applied voltages and laser energies on the breakdown voltage and current waveforms are investigated. The discharge model can accurately predict the measured breakdown voltage curves, despite the existence of discrepancy in quantitatively describing the transient discharge current and voltage waveforms.

Keywords: pulsed laser, photoemission, plasma breakdown, discharge, Paschens curve

(Some figures may appear in colour only in the online journal)

1. Introduction

Plasma discharges have been a topic of continuous great interest because of their numerous applications in surface treatment and spectroscopy, space propulsion, environmental and agricultural fields, and plasma medicine [1–13]. They are widely explored for the development of new technologies [14–16] as well as in commercial ventures [17–21]. On the other hand, continuous efforts are being made to prevent plasma discharge and breakdown in particle accelerators, space communication systems, vacuum electronics, and pulsed power systems [22–27]. The optimisation of plasma technological processes in discharge devices largely depends on plasma breakdown conditions [14].

Laser-induced photoemission of electrons offers opportunities to trigger and control plasmas and discharges [28]. An intense laser pulse can deliver energy to a target surface for a very short interval of time. As a result, instant photoemission, ionisation, and vaporization of the material can take place, depending on the intensity of the laser pulse [28]. At relatively

---

* Authors to whom any correspondence should be addressed.

J. Phys. D: Appl. Phys. **56** (2023) 505204

A Iqbal *et al*

low laser intensity, it induces only photoelectron emission, which initiates or influences the plasma, particularly at low reduced electric fields, E/N, where E and N stand for the electric field and the background gas number density, respectively [29]. However, the effects of laser driven photoemission on the resultant plasmas and discharges are not well understood.

Photoemission itself is a highly nonlinear process through mechanisms including multiphoton absorption, above threshold ionisation, field enhanced hot electron emission, and optical field emission or tunnelling, etc [30]. The dominant process depends on the work function of the material, photon energy and associated optical fields, surface heating, background fields, etc. The mechanisms of laser driven photoemission from metal surfaces have been studied extensively [31–43] with the aid of classical treatment models (i.e. the three-step model [36–39], the Fowler–DuBridge model [32–35], as well as recent quantum mechanical models [30, 40–43]. It is found that both photoemission current and photoelectron energy distribution can be controlled with the laser properties (e.g. laser intensity, laser pulse duration, laser wavelength, laser frequency mixture), material properties, and background fields [30, 40, 41, 44–46]. This offers strong flexibility to control plasmas using photoemission.

Studies have been conducted to measure laser induced plasma properties such as the radiation power density required to cause breakdown [47] and the evolution of plasma temperature [48]. The works of Phelps and Petrovic are notable in the characterisation of laser induced low current discharge oscillations [49, 50]. However, significant gap remains in our understanding of pulsed photoemission induced plasma discharge and breakdown. For instance, the parametric dependence of the breakdown voltage and current on the energy of a pulsed laser as well as the reduced electric field is not clearly characterised.

In this paper, the effect of photoemission on breakdown is characterised. Breakdown experiments are performed and interpreted using a 0D discharge model [49–51] and a quantum model of photoemission [30, 40, 41]. The experimental method for our study is described in section 2. Section 3 presents the model of transient voltage and current in low current discharges. In section 4 we discuss the experimental results and compare them with the predictions of our model. In section 5, we summarise our work and discuss scopes of future work.

2. Experimental method

In this section, we describe the experimental setup and measurement techniques and present the representative transient voltage and current waveforms induced by photoemission.

Figure 1(a) shows a schematic of the experimental setup. Discharges were generated between two parallel aluminium plate electrodes (22 mm × 13 mm) separated by a 3.5 mm gap. The electrodes were enclosed within a vacuum chamber with optical access for imaging using an intensified charge-coupled device (ICCD) and illumination of the cathode by a pulsed

laser source. The flow rate of high-purity (99.9995% pure) argon gas through the vacuum chamber was controlled by a mass flow controller and a programmable interface controller (MKS, 946 Vacuum System Controller) to maintain the desired pressure. The flow rate was kept near 0.3 standard litre per minute at each pressure to avoid accumulation of impurities by adjusting a valve inserted between the vacuum chamber and the vacuum pump (Edwards, nXDS6i). The pressure was monitored using a capacitance manometer (MKS, Baratron) with an accuracy of 0.5% according to the manufacturer. The vacuum chamber was mounted on a translation stage to enable precise alignment with the pulsed laser light.

High voltage feedthroughs on the vacuum chamber were connected to the electrodes to allow for grounding and application of high voltage pulses. A high voltage pulse generator (HVPG) (DEI, PVX-4140) powered by a DC high voltage power supply (Stanford Research Systems, PS325) was connected to the upper electrode in figure 1(a) using a high-voltage co-axial cable and a 1 MΩ current limiting resistor, R_M. The value of R_s is 76 Ω and the capacitance of the co-axial cable was measured with an inductance, capacitance, and resistance (LCR) metre (B&K Precision, 885) and found to be 206 pF, C in figure 1(a). The capacitance of the 1 MΩ resistor and the parallel plate electrodes was measured to be 21 pF. Stray inductance and resistance were too low to be reliably measured by the LCR metre. The HVPG was synced to the pulsed laser source using a delay generator (Stanford Research Systems, DG 535). The voltage on each side of the 1 MΩ resistor, R_M in figure 1(a), was monitored using voltage divider circuits connected to a digital oscilloscope (Teledyne LeCroy, HD06104) with a 1 GHz bandwidth. From these voltage measurements the voltage and current waveforms, $V(t)$ and $I(t)$ in figure 1(a), were calculated, allowing currents as low as 0.5 μA to be determined.

Pulsed laser light was supplied by a tunable laser source (EKSPLA PL2230) consisting of a Nd:YAG laser, optical parametric amplifier, and frequency doubler. The laser was tuned to 230 nm, providing up to 150 μJ of energy per pulse at a repetition rate of 50 Hz and pulse width of 30 ps. The energy of 230 nm photons is 5.4 eV, well above the work function of the electrodes (nominally 4.1 eV for aluminium). Two lenses were used to reduce the spot size of the laser and two mirrors were used to direct the light onto the cathode at an angle of incidence of 19 degrees. The linear polarisation of the light was vertical so that the optical field direction was at an angle of 109 degrees with respect to the cathode surface. The result was an elliptical-like shape on the cathode with a major axis of length 8.3 mm (oriented along the x-dimension, see figure 1(b)) and a minor axis of length 3 mm. The electric field in the gap is uniform over the spatial extent of the laser illumination.

Care was taken to maintain the electrode surfaces. The electrodes were mechanically polished to a mirror finish and thoroughly cleaned with methanol. After placement within the vacuum chamber, the electrodes were kept at pressures lower than 10^{-6} Torr using a turbomolecular pump (Pfeiffer, TMU 261) for at least 48 h. Before each data acquisition, the pulsed

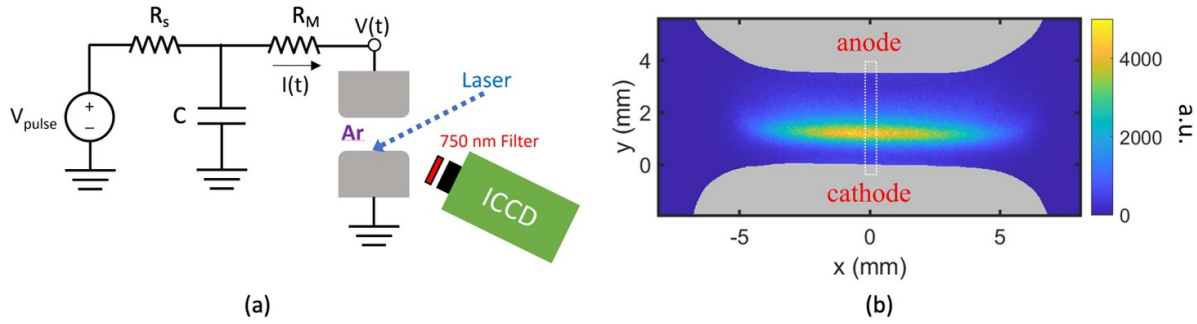J. Phys. D: Appl. Phys. **56** (2023) 505204

A Iqbal *et al*

Figure 1. (a) Schematic of the circuit and optical imaging setup. Pulsed laser light incident on the cathode induces photoemission and plasma breakdown. (b) Linear-scale image of the plate-to-plate discharge acquired with the ICCD at $pd = 1$ Torr cm. The region designated by the dotted white lines was spatially integrated along the x dimension to examine the breakdown evolution.
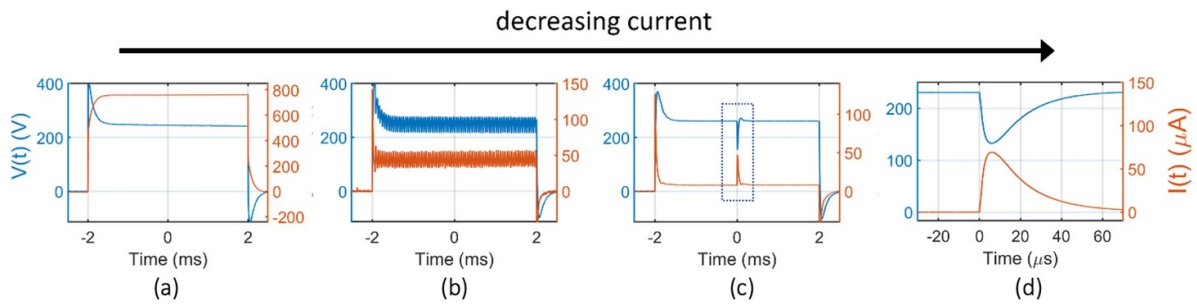

Figure 2. Voltage and current waveforms, $V(t)$ and $I(t)$, respectively, for different drive conditions at $pd = 1$ Torr cm with an applied DC voltage (V_0) of (a) 1000 V, (b) 270 V, (c) 269 V, and (d) 231 V. In (d), the time axis has been zoomed to the region designated by the dotted lines in (c). The effect of pulsed photoemission from the cathode at time 0 ms becomes observable at low currents, as can be seen in (c) and (d).

discharge was operated in argon for at least 15 min (at a repetition rate of 50 Hz), which was observed to provide repeatable discharge conditions. It is to be noted that, during the first 90 s of pulsed discharge operation, with imaging it was possible to observe removal of adsorbed material from the cathode surface by the laser and its subsequent ionisation in the plasma. This effect could not be observed in the current and voltage waveform data.

Figure 1(b) shows an image of the discharge acquired by the ICCD (Andor Technology, iStar DH334T). A 750 nm bandpass filter (Thorlabs, FB750-10) was placed in front of the ICCD to isolate photon emission due to transitions from the argon $2p_1$ state to the $1s_2$ state within the discharge. The $2p_1$ state is excited from the ground state by electrons with an excitation threshold energy of 13.48 eV, close to the first ionisation energy of argon, 15.76 eV. The relation of the excitation rate into the $2p_1$ state and the ionisation rate depends on the relation of the respective cross sections. For the case of electrons having energies less than 17 eV or so the cross sections are of similar value and energy dependence [52], allowing the assumption that imaging of the 750 nm line emission provides a qualitative indication of regions of ionisation within the discharge. For example, considering figure 1(b), most of the ionisation appears to occur above the cathode sheath in the region where the electrons freed from the cathode have gained sufficient energy to excite the $2p_1$ state. Further analysis of the ICCD images is provided below. Scattered laser light does not appear in the image because it is blocked by the

750 nm bandpass filter and the quantum efficiency of the ICCD is close to zero at 230 nm.

Figure 2 shows representative voltage and current waveforms, $V(t)$ and $I(t)$ in figure 1(a), for different current drive conditions at $pd = 1$ Torr cm. The delay generator that controls the HVPG was configured so that the laser pulse arrives 2 ms after the start of a 4 ms long high voltage pulse (time 0 ms in figure 2). The high voltage pulse was applied with a repetition rate of 50 Hz, matching the laser repetition rate. Shot-to-shot memory effects are assumed to be negligible. In figure 2(a), 1000 V DC was supplied to the HVPG, resulting in breakdown of the gas between the electrodes and 758 μA of current. The current can be reduced by decreasing the DC voltage supplied to the HVPG. When the current is sufficiently reduced, oscillations are observed like those shown in figure 2(b). These oscillations can be described by circuit models capturing the nonlinear ionisation and feedback processes in an argon discharge [53]. Oscillations are not a focus of the current study; however, it is to be noted that the discharge conditions could be modified such that the pulsed photoemission at time 0 ms would initiate oscillations, extinguish oscillations, or change the phase of oscillations. Next in figure 2(c), the current was reduced to 8 μA, resulting in a Townsend-like breakdown. At time 0 ms, a surge of current and a drop in voltage is observed that is caused by the electrons freed from the cathode by pulsed photoemission. In figure 2(d), the current was reduced to 0 μA and the surge of current at time 0 ms is still observable. In this case, breakdown was only possible with pulsed photoemission.

J. Phys. D: Appl. Phys. **56** (2023) 505204

A Iqbal *et al*

3. Model of transients in low current discharges with photoemission

To describe the measured transient currents and voltages, we employ the model of transients in low current discharges proposed by Phelps *et al* [50]. In this model, we assume a small space-charge distortion of the electric field in the observed range of currents. The times for significant changes in the electric field and current are assumed to be long compared to the electron and ion transient times.

We also assume that electrons are produced at the cathode only by ions, i.e. contributions from photons (from plasma) and metastables are small. The effective yield of electrons per ion arriving at the cathode is given by:

$$\gamma = \gamma_{\rm p} + k_{\rm V}V + k_{\rm I}I, \tag{1}$$

where $\gamma_{\rm p}$ represents the 'potential ejection' of electrons (i.e. the energy for electron escape is supplied by the potential and not the kinetic energy of the ion [54]), $k_{\rm V}$ is an approximation to the contribution of 'kinetic ejection' of electrons [50], and $k_{\rm I}$ represents first-order effects of space charge on the electric field (and thereby on the electron yield from the cathode) [55, 56]. In this model, ionisation by heavy particles are neglected and only ionisations by electrons are accounted for. Then, the spatial ionisation coefficient (α) is given by [57, 58]:

$$\alpha = Cpe^{-D\sqrt{\frac{p}{E}}}, \tag{2}$$

where p is the gas pressure in Torr, E is the electric field in $\rm V\,cm^{-1}$, and C and D are fitting coefficients for a specific gas ($C = 29.2\,\rm Torr^{-1}\,cm^{-1}$ and $D = 26.6\,\rm V^{1/2}\,Torr^{-1/2}\,cm^{-1/2}$ for argon [14, 57, 59]). If electron and ion currents are considered uniformly distributed over the surface of the electrodes (i.e. the system is one dimensional), then the round-trip electron number gain (g) resulting from an electron released from the cathode becomes a unique function of the gas pressure (p), electrodes separation (d), and discharge voltage (V) [50]:

$$g(t) = \gamma(t)\left[(1+\delta)\,{\rm e}^{\alpha(t)d} - 1\right], \tag{3}$$

where δ represents the yield of ions produced by backscattered electrons, per electron arriving at the anode. With these assumptions, the electron current at the cathode $I_{\rm e}(0, t+T)$ at the time $t+T$ (where T is the ion transit time) is related to the current $I_{\rm e}(0,t)$ at time t and photoelectric current produced by irradiation $I_{\rm p}(0,t)$ by [50]:

$$I_{\rm e}(0,t+T) = I_{\rm p}(0,t+T) + \gamma I_{\rm e}(0,t)\left[{\rm e}^{\alpha(t)d} - 1\right]$$
$$+ \delta\gamma I_{\rm e}(0,t)\,{\rm e}^{\alpha(t)d}. \tag{4}$$

Using Taylor's expansion, $I_{\rm e}(0,t+T) = I_{\rm e}(0,t) + T\frac{{\rm d}I_{\rm e}(0,t)}{{\rm d}t}$, we can eliminate $I_{\rm e}(0,t+T)$ in equation (4) as follows:

$$\frac{{\rm d}I_{\rm e}(0,t)}{{\rm d}t} = \frac{I_{\rm p}(0,t)}{T} + \frac{[g-1]}{T}I_{\rm e}(0,t). \tag{5}$$

The electron current emitted from the cathode is given by:

$$I_{\rm e}(0,t) = \gamma I_{+}(0,t), \tag{6}$$

where $I_{+}(0,t)$ is the positive ion current. Therefore, the total current $I = I_{\rm e} + I_{+}$ is related to the electron current $I_{\rm e}(0,t)$ at the cathode by:

$$\frac{I}{I_{\rm e}(0,t)} = \frac{1+\gamma}{\gamma}. \tag{7}$$

Combining equations (1), (5), (6), and (7) we obtain Phelps's discharge characteristic equation [50]:

$$\frac{{\rm d}I}{{\rm d}t} = \left[\frac{(1+\gamma)I_{\rm p}}{\gamma T} + \frac{(g-1)I}{T} - \frac{Ik_{\rm V}}{\gamma(1+\gamma)}\frac{{\rm d}V}{{\rm d}t}\right]$$
$$\times \left[1 + \frac{Ik_{\rm I}}{\gamma(1+\gamma)}\right]^{-1}. \tag{8}$$

The discharge voltage $V(t)$ can be expressed in terms of the discharge current $I(t)$ and the circuit components shown in figure 1(a) as—

$$\frac{{\rm d}V}{{\rm d}t} = \frac{1}{R_{\rm s}C}\left[V_0 - V - I(R_{\rm s} + R_{\rm m})\right] - R_{\rm m}\frac{{\rm d}I}{{\rm d}t}. \tag{9}$$

The coupled equations (8) and (9) are used to model the transient voltages and currents due to pulsed photoelectron emission current induced by lasers on the cathode. It is important to note that the discharge characteristic equation assumes the time scale of change for current and voltages is long compared to electron (ion) transient time, i.e. $\sim 10^{-10}$ s ($\sim 10^{-6}$ s) for the given experimental conditions. Thus, it is incapable of handling the ultrafast details of the photoemission current from the cathode illuminated by the laser pulses, where the photoelectric current pulse length is on the order of the laser pulse length [30] (i.e. ~ 30 ps in the experiment), much smaller than the electron transit time. In order to still use equations (8) and (9) to model the plasma behaviours, we have to neglect the detailed time dependence of the photocurrent and are only concerned with the integrated effect of the very short pulse, following Phelps *et al* [50]. This is also implied in the derivation of equation (5), where we have assumed $I_{\rm p}(0,t) = I_{\rm p}(0,t+T)$, because the time scale of change of quantities, including $I_{\rm p}$, has to be on the order of T, as constrained by the Taylor's expansion $I_{\rm e}(0,t+T) = I_{\rm e}(0,t) + T\frac{{\rm d}I_{\rm e}(0,t)}{{\rm d}t}$ that we applied. Thus, both photocurrent $I_{\rm p}$ and its duration τ are adjusted as fitting parameters to best fit the measured current–voltage (*IV*) curves for a given set of voltage and laser conditions [49]. The resulting time variations of *IV* curves are caused by the transfer of the photoelectron charge per laser pulse $Q_{\rm t} = \int_0^\tau I_{\rm p}{\rm d}t$ (pC), which is compared with the total photoelectron charge emission from the quantum model for photoemission [30, 40].

The quantum model for photoemission is based on the exact analytical solution of the time-dependent Schrodinger equation subject to the oscillatory surface barrier due to the

J. Phys. D: Appl. Phys. **56** (2023) 505204

A Iqbal *et al*

combined laser field and background field [30, 40, 41], from which the emission current density J can be calculated by

$$J = e \int_0^\infty D(\varepsilon) N(\varepsilon) \, \mathrm{d}\varepsilon, \tag{10}$$

where $N(\varepsilon) = \frac{mk_B T_e}{2\pi^2 \hbar^3} \ln[1 + \exp(\frac{E_F - \varepsilon}{k_B T_e})]$ is the supply function derived from the free electron model for metal, with E_F, k_B, and T_e being the Fermi level, the Boltzmann constant, and the temperature, respectively, and $N(\varepsilon) \, \mathrm{d}\varepsilon$ gives the flux of electrons inside the metal imping normal on the metal surface with initial energy between ε and $\varepsilon + \mathrm{d}\varepsilon$. The electron emission probability from energy level of ε is,

$$D(\varepsilon) = \sum_{n=-\infty}^{\infty} w_n(\varepsilon), \tag{11}$$

where $w_n(\varepsilon)$ denotes the electron transmission probability through n-photon process, with $n < 0$ representing multiphoton emission process, $n = 0$ direct tunnelling process, and $n > 0$ multiphoton absorption process. The detailed expressions for $w_n(\varepsilon)$ can be found in [40, 41]. The total emitted photoelectron charge per laser pulse is integrated over the laser pulse length as $Q_e = \int_0^{\tau_{laser}} JA \mathrm{d}t$ (pC), with A being the emission area.

4. Results and discussion

In this section, the laser induced transient voltage and current waveforms are analysed together with streak images. The effects of different applied voltages and laser energies on the breakdown voltage and current waveforms are discussed. The experimental measurements are compared with numerical results.

Figure 3 shows the temporal evolution of the pulsed photoemission induced breakdown. The measured waveforms (solid lines) in figure 3(a) are the same as in figure 2(d). The 'streak images' in figures 3(b) and (d) were formed by spatially integrating the region designated by the dotted lines in figure 1(b) along the x dimension. Transient current and voltage waveforms obtained from numerical calculations (dotted curves) using equations (8) and (9) are also shown in figures 3(a) and (c). Empirical values of discharge parameters are used in the numerical calculations to fit the measured discharge currents (see appendix A for further discussion of the discharge parameters used in the numerical calculations). For convenience of later discussions, we define the parameters V_{min} and I_{max} as the minimum and maximum values of $V(t)$ and $I(t)$, respectively (shown in figures 3(a) and (c)), within the time range of 0 to 100 μs of each scope trace.

Considering first $pd = 1$ Torr cm in figures 3(a) and (b), during the arrival of the 30 ps laser pulse at time, $t = 0$ μs, electrons are emitted from the cathode (bottom electrode shown in grey in figure 3(b)) and then accelerated across the gap. These electrons attain sufficient energy to ionise the gas and ionisation growth by electron avalanche is observed in the region

nearer to the anode. The ions then drift towards the cathode, changing the potential across the gap and forming a cathode sheath. Secondary electron emission by (primarily) ions supplies new electrons that are accelerated across the sheath and ionise the gas. After about 1 μs, the sheath begins to grow and eventually the current decreases and the breakdown is extinguished because the applied voltage across the gap is too low to allow generation of one electron for each electron lost. A similar breakdown evolution is observed at $pd = 10$ Torr cm in figure 3(d), however the time step has been decreased from 250 ns in figure 3(b) to 50 ns in figure 3(d), capturing the formation of a striated anode column that does not appear at $pd = 1$ Torr cm. The formation of the anode column corresponds to the formation of the cathode sheath. It is to be noted that the light emission from the region directly above the cathode that appears to be located within the sheath (especially noticeable between time 0.2 and 0.5 μs in figure 3(d)) is an artefact caused by the imaging optics and surface reflections and should be ignored. Such artefacts also appear in figures 6 and 7.

Figure 4 shows the transient current (figures 4(a) and (c)) and voltage (figures 4(b) and (d)) waveforms for different amplitudes (V_0) of the applied DC voltage (i.e. V_{pulse} in figure 1(a)) obtained from the experimental measurements (solid curves) and numerical calculations (dotted curves) for $pd = 1$ Torr cm (top row) and 10 Torr cm (bottom row) when a 230 nm (5.39 eV), 36 μJ pulsed laser is incident on the cathode at time, $t = 0$ μs. In the numerical calculation, the photoelectric current (I_p) produced by irradiation is approximated with a Gaussian shaped simulation pulse. The total transferred photoelectron charge $Q_t = \int_0^\tau I_p \mathrm{d}t$ (pC) for different applied DC voltages are given in tables 1 and 2 for $pd = 1$ and 10 Torr cm, respectively.

Figure 4(a) shows that the value of I_{max} (described in figures 3(a) and (c)) decreases as the DC voltage supplied to the HVPG (V_0) decreases. We also observe that at $pd = 10$ Torr cm (figure 4(c)) a larger $V_0(> 300$ V) is required to obtain pulsed photoemission induced breakdown compared to those in figure 3(a) for $pd = 1$ Torr cm and the corresponding values of I_{max} are also higher. From figure 4(b), we observe that as V_0 increases, the value of V_{min} (described in figures 3(a) and (c)) first increases for $151 \leqslant V_0 \leqslant 191$ V and then decreases for $V_0 > 191$ V. This is because at $V_0 \sim 190$ V, a transition from a Townsend to glow discharge occurs resulting in a significant increase in the discharge current and a decrease in the value of V_{min}. This transition is more obvious in figures 4(c) and (d) at $V_0 \sim 310$ V. This will be further discussed in figures 6 and 7.

For $pd = 1$ Torr cm, $V_0 < 191$ V as well as for $pd = 10$ Torr cm, $V_0 < 320$ V, the measured current amplitudes (figures 4(a) and (c)) and the corresponding charge transfer (tables 1 and 2) are quite low compared to the other current amplitudes (figures 4(a) and (c)) and charge transfer (tables 1 and 2) values. This is because $V_0 < 191$ V for $pd = 1$ Torr cm and $V_0 < 320$ V for $pd = 10$ Torr cm represent the pre-breakdown regimes of the discharge (i.e. the applied voltage < breakdown voltage), which will be further discussed in figures 6 and 7.
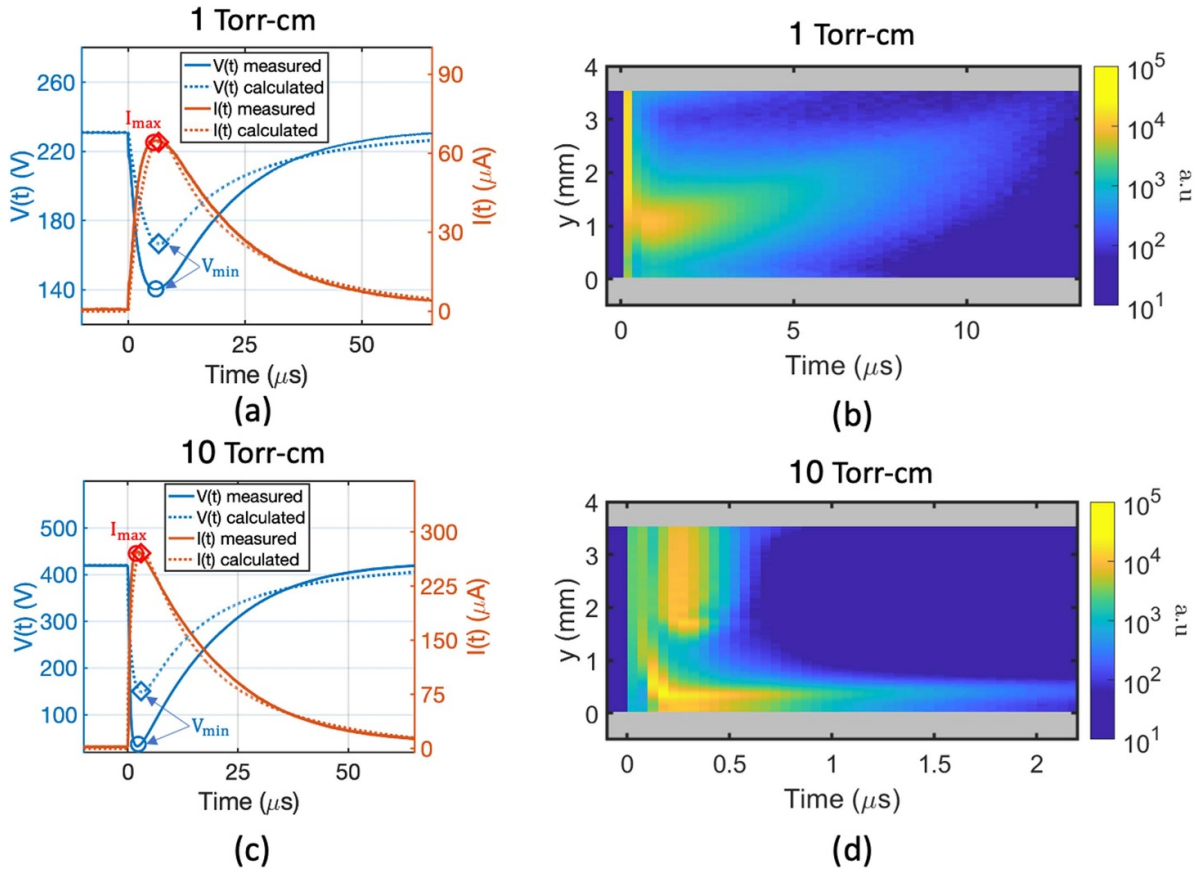
Figure 3. (a), (b): Temporal evolution of the pulsed photoemission induced breakdown for $pd = 1$ Torr cm; (a) $V(t)$ and $I(t)$ waveforms obtained from experimental measurements (solid curves) and numerical calculations (dotted curves) using equations (8) and (9); (b) streak image formed by spatially integrating the region designated by the dotted lines in figure 1(b) along the x dimension. (c), (d): same plots as those of (a), (b) for $pd = 10$ Torr cm. Minimum values of $V(t)$ (blue circles for measured values and blue diamonds for values obtained from numerical calculations) and maximum values $I(t)$ (red circles for measured values and red diamonds for values obtained from numerical calculations) are labelled in (a) and (c) as $V_{\min}$ and $I_{\max}$, respectively. Note the different time scales in (b) and (d).

The charge transfer due to photocurrent pulse (I_p) needed to fit the measured current amplitude for $pd = 10$ Torr cm for voltage $V_0 \geqslant 320$ V (figure 4(c)) is much higher than that for $pd = 1$ Torr cm (figure 4(a)), as seen from tables 1 and 2. This is because the measured current amplitudes for $pd = 10$ Torr cm (solid curves in figure 4(c)) are much higher than those for $pd = 1$ Torr cm (solid curves in figure 4(a)), which may be attributed to the higher breakdown voltages (assuming $R_s \gg R_{\text{plasma}}$, the internal plasma resistance), more photoelectron charges emitted due to plasma irradiation of the surface at higher applied voltages, and the higher gas number density (N) at $pd = 10$ Torr cm resulting in a higher number of electrons produced per unit time under similar voltages, $k_i N$, where k_i is the rate coefficient for ionisation. In addition, according to equation (2) and the assumption of the 0D model that the voltage drop occurs uniformly across the gap, the first Townsend ionisation coefficient (α) for the applied DC voltages is smaller at $pd = 10$ Torr cm than at $pd = 1$ Torr cm. Thus, the model requires higher values of I_p and $\int_0^\tau I_p dt$ to match the breakdown data at higher pd.

It is also noteworthy from table 1 that a small charge transfer (10^{-12} C to 10^{-13} C) due to photocurrent pulse (I_p) is necessary to fit the observed current amplitude for $pd =$

1 Torr cm (figures 3(a) and 4(a)), which is much smaller than the emitted charge due to photoemission from the cathode (2.1033×10^{-10} C) calculated from equations (10) and (11), the quantum model of photoemission [30, 40]. Similar observation was previously made by Petrović and Phelps [49]. However, the values of $\int_0^\tau I_p dt$ for $pd = 10$ Torr cm with $V_0 \geqslant$ 320 V (from table 2), are of the same order of magnitude as the emitted charge calculated from the quantum model of photoemission (i.e. 2.1033×10^{-10} C). The discrepancy between the fitted charge transfer and emitted charge from photoemission might be caused by the limitations of the 0D transient model: it does not differentiate between the convection current in the gap and the induced current in the electrodes according to the Ramo-Shockley theorem [60, 61]; it assumes that the voltage drop and electron multiplication occurs uniformly across the gap although in reality it takes place primarily across the cathode sheath; it does not account for the spatial nonuniformity of the electric field across the gap which can be very different for different pd values (especially at high currents when the electric field may experience significant space-charge distortion); it cannot account for the details of the ps-scale photoemission current. In addition, the assumed linear dependence of γ on $V(t)$ and $I(t)$ in equation (1) may not be universally

J. Phys. D: Appl. Phys. **56** (2023) 505204
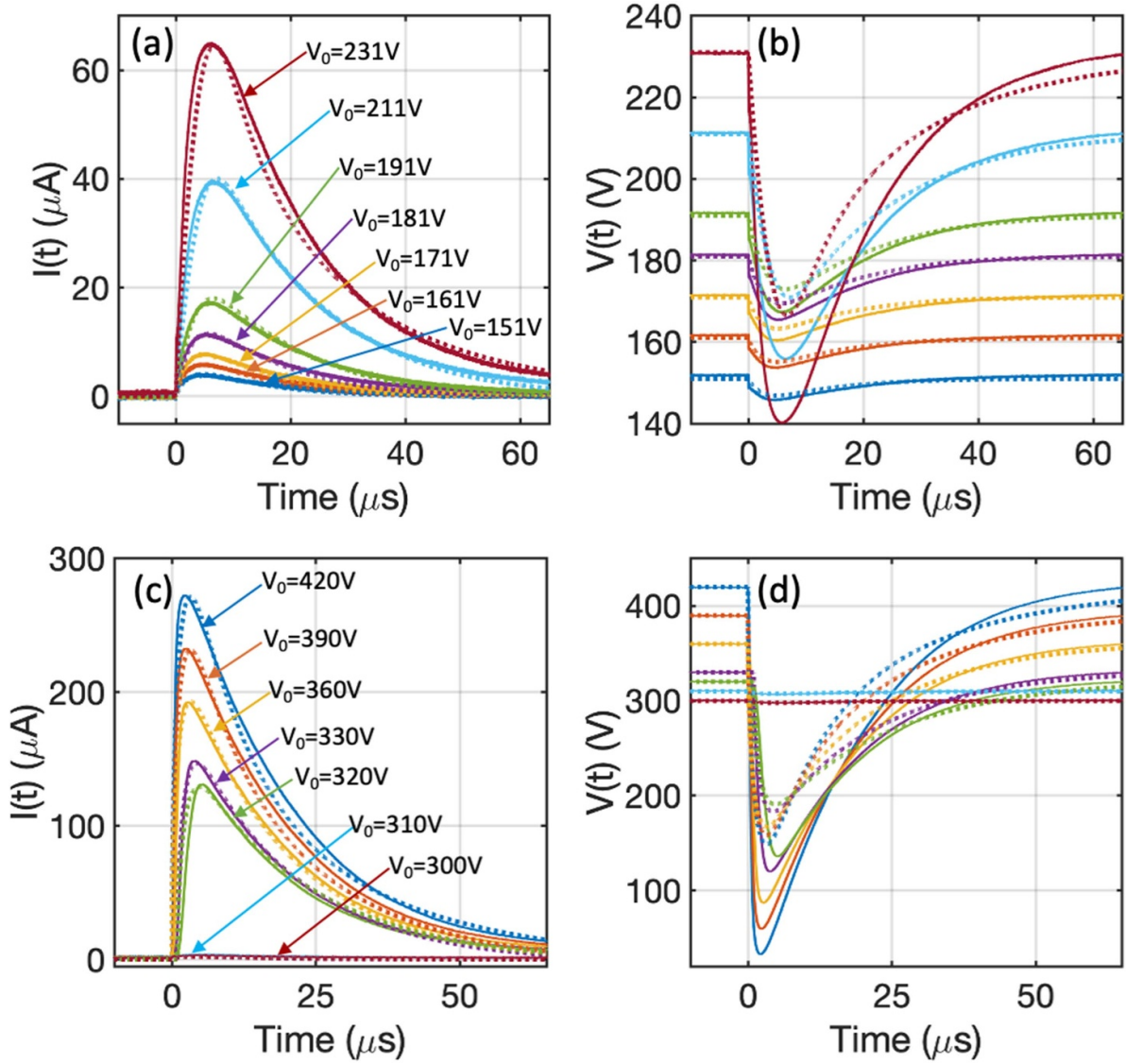
A Iqbal *et al*

Figure 4. Top row: transient (a) current and (b) voltage waveforms for $pd = 1$ Torr cm resulting from the photoemission due to a 230 nm (5.39 eV), 36 μJ pulsed laser incident on the cathode at time $t = 0$ μs, with different amplitudes of the applied voltage pulse, V_0. The solid curves are obtained from the experiments described in section 2 with $C = 206$ pF, $d = 0.35$ cm, $R_s = 76$ Ω and $R_M = 1$ MΩ, respectively. The dotted curves are the results of calculations using equations (8) and (9). Bottom row: transient (c) current and (d) voltage waveforms for $pd = 10$ Torr cm with the same parameters as those in the top row. Note that in (c), the discharge current waveform for $V_0 = 300$ V is almost completely overlaid on the discharge current waveform for $V_0 = 310$ V.

Table 1. Photoelectron charge transferred during the Gaussian-shaped I_p with pulse-width of $\tau = 25$ μs and $pd = 1$ Torr cm.

Applied voltage (V)	231	211	191	181	171	161	151
$\int_0^\tau I_p dt$ (pC)	5.04	3.59	1.54	0.908	0.567	0.425	0.284

Table 2. Photoelectron charge transferred during the Gaussian-shaped I_p with pulse-width of $\tau = 25$ μs and $pd = 10$ Torr cm.

Applied Voltage (V)	420	390	360	330	320	310	300
$\int_0^\tau I_p dt$ (pC)	115.9	109.7	97.26	70.3	45.5	0.124	0.104

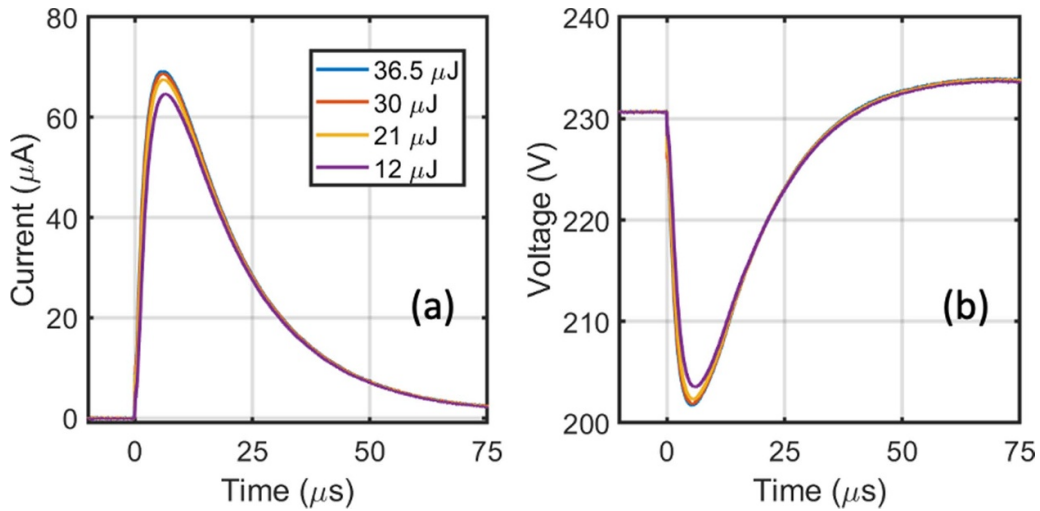J. Phys. D: Appl. Phys. **56** (2023) 505204

A Iqbal *et al*

Figure 5. Measured transient (a) current and (b) voltage waveforms due to different energies, $E_{\text{Laser}} = 12, 21, 30,$ and 36.5 μJ, of a pulsed laser incident on the cathode at time $t = 0$ μs. Here, $pd = 1$ Torr cm and applied DC voltage amplitude, $V_0 = 231$ V.

applicable for different pd values, thus affecting the quantitative results. Further studies with higher spatiotemporal fidelity models, such as Monte Carlo [62, 63], kinetic (convective scheme) [64], and particle in cell (PIC) [65], are required to resolve these issues.

Differences between the discharge voltage waveforms (figures 3(a), (c) and 4(b), (d)) obtained from experimental measurements (solid curves) and numerical calculations (dotted curves) can also be largely attributed to the simplifying assumptions of the 0D transient model (as described above) [50]. In addition, the voltage source in the experiment, V_{pulse}, consists of a parasitic capacitance, the value of which may vary with time due to the feedback from the external circuit components (see appendix B for detailed discussion). Such temporal fluctuation of the source capacitance can also contribute to the difference between the calculated and measured discharge voltages. We shall show in appendix B that the temporal variation of the parasitic source capacitance is maximum near the extremum values of the transient voltage and current profiles. It is, therefore, noteworthy that when the extremum values of the transient voltage and current profiles have small excursions from their steady state values (i.e. for small amplitude of the applied DC voltages $V_0 \leqslant 161$ V in figure 4(b) and $V_0 \leqslant 310$ V in figure 4(d)), the transient voltage profiles obtained from numerical calculations show a relatively better agreement with their experimentally measured counterparts.

Figure 5 shows the measured transient current and voltage waveforms with different energies of the incident laser pulse ($E_{\text{Laser}} = 12, 21, 30,$ and 36.5 μJ). We observe from figure 5 that the effect of the laser energy on pulsed photoemission induced breakdown is much less prominent than the effect of the applied DC voltage amplitude (i.e. top row of figure 4). To understand the reason for this, we employ a quantum model of photoemission [30, 40, 42] and estimate the total emitted charge (Q_e) through photoemission using equations (10) and (11) when a laser pulse is incident on an aluminium

surface. To align with the quantum model with a surface barrier under a perpendicular laser field to the surface, we use the orthogonal component of the laser field (19 degrees incident angle) and an elliptical emission area as described in the experimental setup in section 2. We find the total emitted charge, $Q_e = 7.0109 \times 10^{-11}, 1.2269 \times 10^{-10}, 1.7527 \times 10^{-10},$ and 2.1325×10^{-10} C for $E_{\text{Laser}} = 12, 21, 30,$ and 36.5 μJ respectively (i.e. as E_{Laser} increases from 12 to 36.5 μJ, Q_e increases by approximately 3.04 times). Fitting the curves in figure 5 using the transient model equations (8) and (9) gives the transferred photoelectron charge $Q_t = 4.92, 5.35, 5.5,$ and 5.6 pC approximately, for $E_{\text{Laser}} = 12, 21, 30,$ and 36.5 μJ, respectively (i.e. as E_{Laser} increases from 12 to 36.5 μJ, Q_t increases by approximately 1.14 times, close to that estimated by the quantum model). For higher laser intensity, in addition to the increased optical field to suppress the surface barrier to increase electron emission, the laser heating also promotes more electrons to higher energy levels, resulting in a higher probability of emission and therefore a higher emitted charge [30].

Figure 6 shows the voltage dependence of breakdown at $pd = 1$ Torr cm without (top row) and with (bottom row) pulsed photoemission. The DC voltage supplied to the HVPG was varied in 10 V steps from 500 to 60 V. Images were acquired with integration times of 50 μs, integrating the temporal variation shown in figure 3(b). Images and scope traces were acquired at times before and during the pulsed photoemission to allow for comparison and repeatable electrode conditions.

Considering the case of no pulsed photoemission in figures 6(a) and (b), the current decreases linearly and the voltage decreases slightly as the DC voltage supplied to the HVPG is decreased from 500 V, corresponding to the regime shown in figure 2(a). From 270 to 240 V oscillations like in figure 2(b) appear. At 230 V and below, the current is 0 μA, V_{min} equals the DC voltage supplied to the HVPG, and no breakdown occurs. Similar conclusions can be drawn
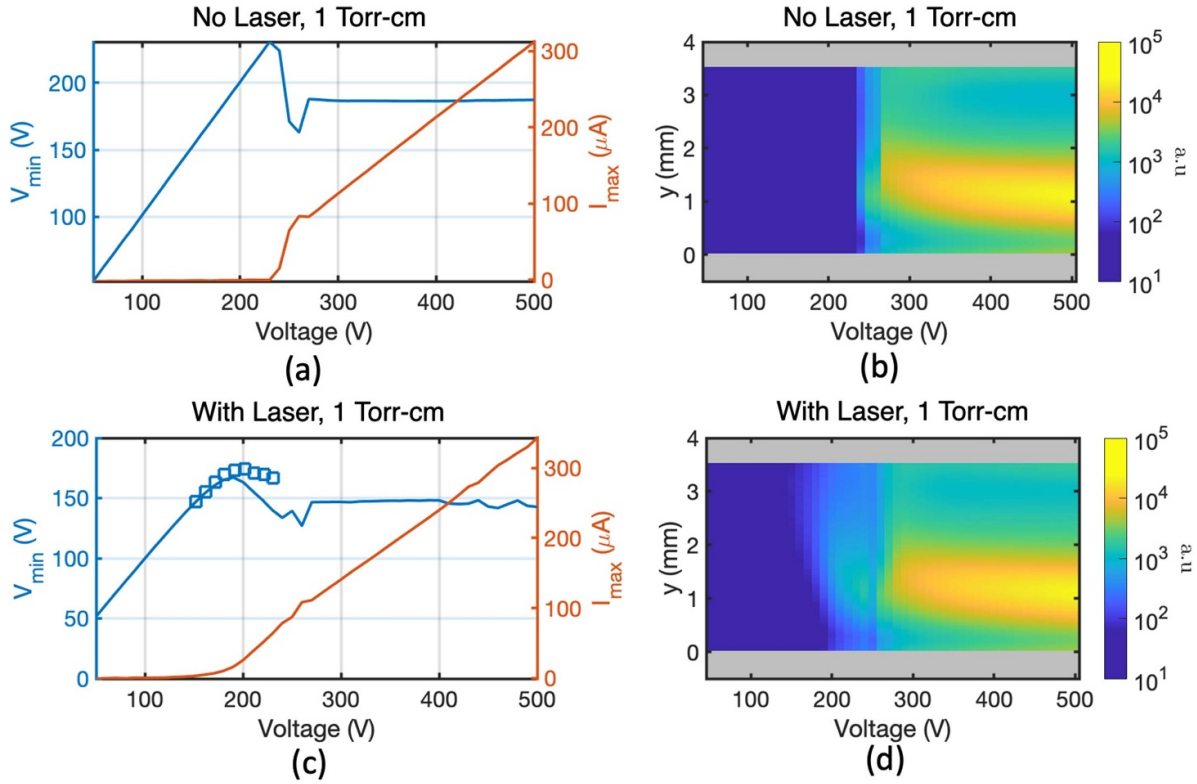
Figure 6. Top row: (a) measured values of V_{min} and I_{max} (as defined in figure 3) for different DC voltages (V_0) supplied to the HVPG for $pd = 1$ Torr cm without pulsed photoemission, (b) corresponding streak images acquired with integration times of 50 μs, integrating the temporal variation shown in figure 3(b). Bottom row: same figures as those in the top row, with pulsed photoemission. Blue diamond shaped markers in (c) shows the V_{min} values obtained from numerical calculations in figure 4(b).

from figure 6(b) which shows the growth of the cathode sheath with decreasing voltage until below 235 V when no breakdown occurs. Therefore, we can consider the minimum voltage required for breakdown without pulsed photoemission at $pd = 1$ Torr cm to be 235 ($\pm$5) V, consistent with previous measurements [29]. It is to be noted that Townsend-like breakdown like in figure 2(c) never occurred when stepping the voltage. This type of breakdown could only be achieved by slowly and carefully adjusting the voltage in a continuous manner by hand.

Next, considering the case of pulsed photoemission in figures 6(c) and (d), there is a similar trend as in figures 6(a) and (b) except that breakdown occurs at voltages less than 230 V, and this breakdown is like that shown in figure 3(b). For this case of $pd = 1$ Torr cm, it is difficult to define the minimum voltage required for breakdown as the current appears to exponentially decay to 0 μA and (within the precision of the measurements) reaches 0 μA at 110 V. However, V_{min} begins to trend downwards between 180 and 190 V. We observe from figure 6(d) that unlike figure 6(b) (and figure 7(d), discussed below), a transition from glow to Townsend discharge with decreasing voltage is not abrupt in this case. Figure 6(d) shows that the streak image starts resembling a more Townsend-like breakdown at approximately 185 V. Therefore, we can consider the minimum voltage required for breakdown with pulsed photoemission at $pd = 1$ Torr cm to be 185 ($\pm$5) V. It is also noteworthy that although the calculated values of V_{min}

with the laser (blue diamond shaped markers in figure 6(c) obtained from the waveforms in figure 4(b)) differ from their experimentally measured counterparts, the breakdown voltage obtained from the numerical calculation ($\sim$190 V) agrees well with the measured breakdown voltage in figure 6(c). We show below that this value is consistent with other pd values where the transition to Townsend-like breakdown is less ambiguous.

Figure 7 shows the voltage dependence of breakdown at $pd = 10$ Torr cm without (top row) and with (bottom row) pulsed photoemission. The same trends appear as in figure 6, and we find the minimum voltage required for breakdown without pulsed photoemission to be 425 ($\pm$5) V. Comparing figures 7(c) and (d) to figures 6(c) and (d), the transition to Townsend-like breakdown with decreasing voltage is clear and occurs at 315 ($\pm$5) V. This value agrees with the breakdown voltage obtained from the numerical calculation using equations (8) and (9), i.e. blue diamond shaped markers in figure 7(c) obtained from the waveforms of figure 4(d).

Currently, we do not have an explanation for why the transition to Townsend-like breakdown occurs differently for 1 and 10 Torr cm. Some differences are observed between the two cases. Considering figures 7(a) and (b), at voltages where oscillations like in figure 2(b) occur ($420 - 480$ V), a striated positive column appears that is not present in figure 6. Considering this same voltage range in figures 7(c) and (d), the pulsed photoemission appears to influence the striations. For voltages less than 420 V in figures 7(c) and
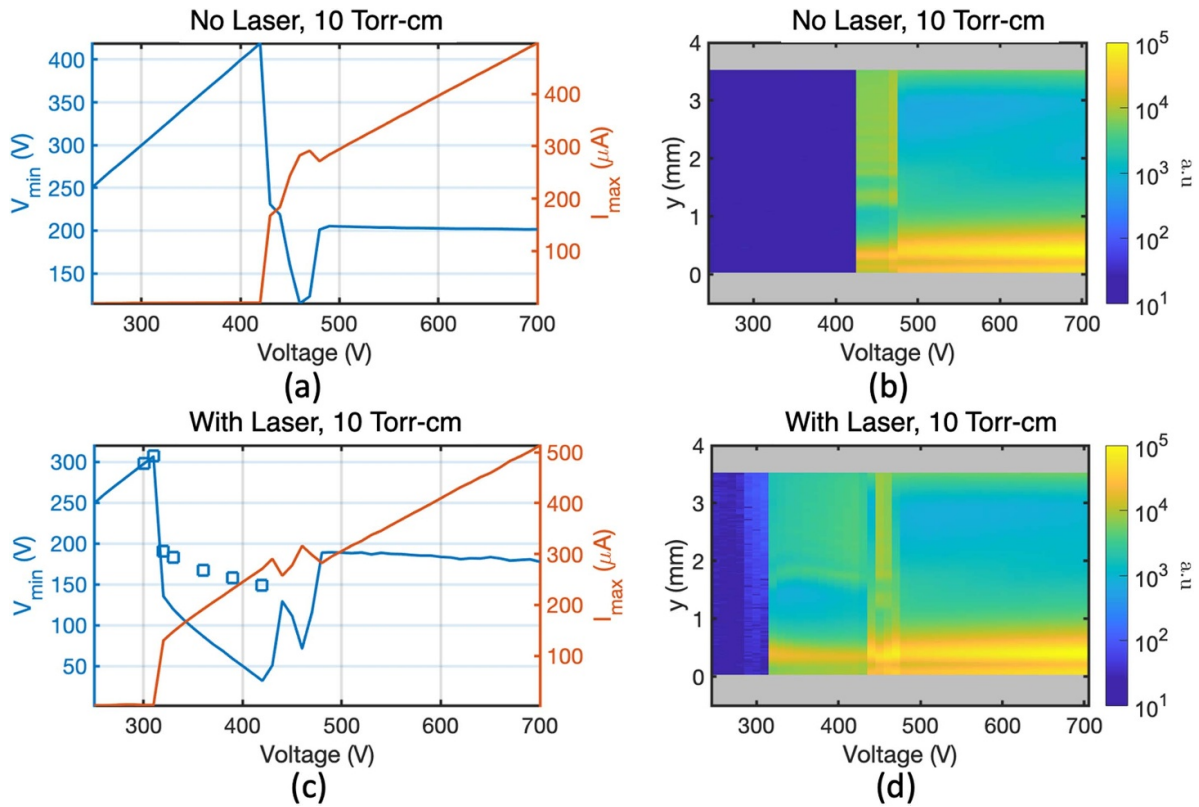
Figure 7. Top row: (a) measured values of $V_{\min}$ and $I_{\max}$ (as defined in figure 3) for different DC voltages (V_0) supplied to the HVPG for $pd = 10$ Torr cm without pulsed photoemission, (b) corresponding streak images acquired with integration times of 50 μs, integrating the temporal variation shown in figure 3(d). Bottom row: Same figures as those in the top row, with pulsed photoemission. Blue diamond shaped markers in (c) shows the $V_{\min}$ values obtained from numerical calculations in figure 4(d).
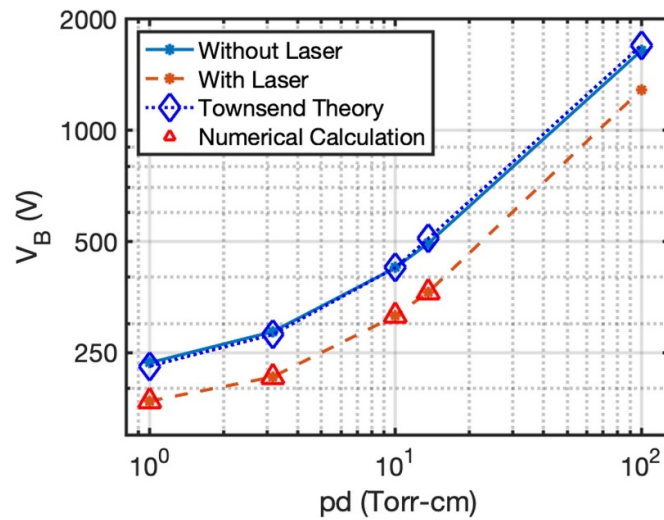

Figure 8. Minimum voltage required for breakdown, V_B, with and without pulsed photoemission at the cathode as a function of pd. The blue dotted curve with diamond markers is obtained by solving Townsend breakdown criterion (equation (A1) in appendix A) with secondary electron emission coefficient, $\gamma = 0.005$ (approximated from equation (1) with the empirical values of k_V and k_I for $pd = 1$ Torr cm described in appendix A), $C = 29.2$ Torr^{-1} cm^{-1} and $D = 26.6$ V$^{1/2}$ Torr$^{-1/2}$ cm$^{-1/2}$ [57].

(d), the breakdown is like that shown in figure 3(d) and includes a striated positive column. Exponential decrease in $I_{\max}$ below 420 V, as observed in figure 6(c), may still occur but is not observed due to the 10 V sampling steps.

Finally, figure 8 plots the minimum voltage required for breakdown, V_B, with and without pulsed photoemission for different values of pd. For pd values of 1, 3.16, 10, 13.6, and 100 Torr cm, V_B was 235, 285, 425, 495, and 1645 V, respectively, without pulsed photoemission, and

J. Phys. D: Appl. Phys. **56** (2023) 505204

A Iqbal *et al*

185, 215, 315, 365, and 1290 V, respectively, with pulsed photoemission. Plotted on a logarithmic scale in figure 8, the pulsed photoemission is shown to shift the 'Paschens curve' downwards. The V_B with photoemission is consistently about 75% of the breakdown voltage without photoemission.

It is noteworthy that equation (1) assumes that the yield of electrons is determined by the discharge voltage *V*, as would be the case for discharges where the positive ions cross the discharge under free-fall conditions. Such an assumption is appropriate only for low-pressure discharges [50]. Therefore, the transient model has not been applied to $pd = 100$ Torr cm in figure 8.

5. Conclusion and future works

In summary, this article characterises pulsed photoemission induced breakdown in argon plasma. At low currents ($<100\ \mu$A), laser induced photoemission can be sufficiently de-coupled from space charge effects to be observable. Photoemission induced plasma breakdown is investigated with high-speed imaging for different reduced electric fields and laser intensities, using a tunable picosecond laser. The laser-induced breakdown voltage was found to be lower than the Townsend breakdown voltage. The effect of the laser energy on transient waveforms of the voltage and current is found to be less prominent than the effect of the applied DC voltage amplitude.

Phelps's circuit model and a quantum model of photoemission are employed to interpret the experimental measurements. Numerical calculations with the simple 0D discharge model can accurately predict the breakdown voltage curve as well as qualitatively explain the relative effects of the applied DC voltage and the laser energy on breakdown. However, it falls short in terms of quantitatively describing the transient voltage and current waveforms, even with empirical approximations, implying the necessity for a higher fidelity model.

Higher order effects of photoemission are difficult to capture in modelling in the present study. Higher dimensional kinetic models may be needed to address this issue in place of the 0D discharge characteristics equation. Another major disadvantage of the 0D discharge model used in this work is its inapplicability for high pressure discharges and ions with large charge-transfer cross sections due to the simplified assumptions made in equation (1) [50]. To overcome these limitations, future studies may focus on simulations in higher dimensions.

Although pulsed photoemission in our experiments induced breakdown and formed a plasma sheath, the applied voltage was found to be insufficient for secondary electron emission to maintain the plasma. Finding methods to sustain pulsed photoemission induced plasma for longer durations, e.g. using multiple consecutive laser pulses, might be interesting for various plasma applications.

Appendix A. Discharge parameters

As per Townsend breakdown criterion, the product of the excess electron multiplication and the yield equal unity, i.e.

$$\gamma = \frac{1}{e^{\alpha d} - 1}. \tag{A1}$$

We employ this condition to obtain empirical values of γ corresponding to experimentally measured breakdown voltages without laser (solid blue curve in figure 8). A linear approximation to the γ values subsequently yields $k_V = \frac{\partial \gamma}{\partial V} = 1.4688 \times 10^{-5}$ V^{-1} for $pd = 1$ and 10 Torr cm. The following empirical expressions of k_I are used to fit the measured current waveforms in figures 3 and 4.

$$k_I = 0.0072(E/N)^2 - 10.4\,(E/N) + 3814;\ pd = 1 \text{ Torr cm}. \tag{A2}$$

$$k_I = 0.0043(E/N)^2 - 10.7\,(E/N) + 6814;\ pd = 10 \text{ Torr cm}. \tag{A3}$$

Here (E/N) has the unit Td.

Ion drift velocity (in cm/s) is estimated with the following empirical expressions -

$$v_d = 337.9 + 0.1702\,(E/N)\,;E/N \leqslant 612 \text{ Td} \tag{A4}$$

$$v_d = 5.13 \times 10^{-14} e^{0.05(E/N)} + 336.6 e^{0.00051(E/N)};$$
$$E/N > 612 \text{ Td}. \tag{A5}$$

The ion transit time is then estimated as $T = d/v_d$ (ranging from $5 - 12\ \mu$s at different applied electric fields for the given experimental conditions).
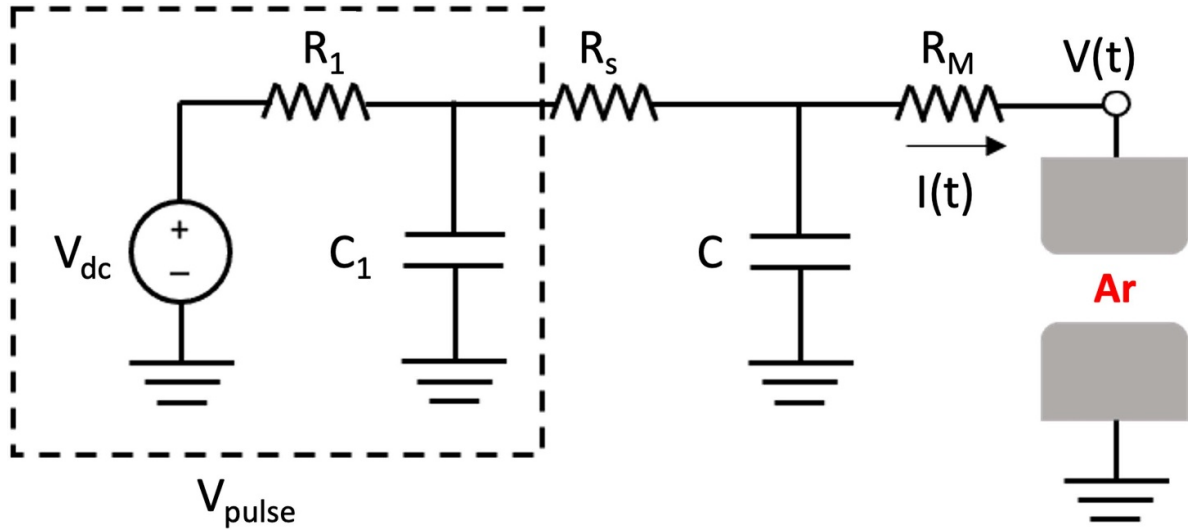
Figure 9. Schematic of the circuit with the high voltage pulse generator, V_{pulse}, of figure 1 replaced by the components inside the dashed rectangle, i.e. V_{dc}, R_1, and C_1.

Appendix B. Parasitic capacitance in the high voltage pulse generator (HVPG)

Figure 9 shows the schematic of the circuit of figure 1 with the high voltage pulse generator, V_{pulse}, replaced by a DC voltage source (V_{dc}), a source resistance (R_1), and a source capacitance (C_1). Prior to the circuit connection, the values of R_1 and C_1 are measured to be 50.9 Ω and 0.29 μF, respectively. While connected to the circuit, the value of C_1 can be estimated in terms of $I(\text{t})$ and $V(\text{t})$ as follows.

$$C_1 = \frac{[V_{\text{dc}} - V(t) - I(t)(R_1 + R_{\text{s}} + R_{\text{m}})] - [CR_{\text{m}}R_{\text{s}} + R_1CR_{\text{m}}]\frac{\text{d}I(t)}{\text{d}t} - [R_{\text{s}}C + R_1C]\frac{\text{d}V(t)}{\text{d}t}}{R_1CR_{\text{s}}\frac{\text{d}^2V(t)}{\text{d}t^2} + R_1\frac{\text{d}V(t)}{\text{d}t} + R_1R_{\text{s}}CR_{\text{m}}\frac{\text{d}^2I(t)}{\text{d}t^2} + (R_1R_{\text{s}} + R_1R_{\text{m}})\frac{\text{d}I(t)}{\text{d}t}}. \tag{B1}$$

Using $C = 206$ pF, $d = 0.35$ cm, $R_{\text{s}} = 76$ Ω and $R_{\text{M}} = 1$ MΩ, (as described in section 2) and the measured values of $I(\text{t})$ and $V(\text{t})$ from figures 4(a) and (b), we find from equation (B1) that the source capacitance, C_1, changes with time as a function of $I(\text{t})$, $V(\text{t})$, and V_{dc} (figure 10). While for a long period during the circuit operation (i.e. time $\geqslant 10$ μs), C_1 remains close to its measured value prior to the circuit connection (0.29 μF), it shows significant deviation from that value while the measured $I(\text{t})$ and $V(\text{t})$ are near their extremum values (i.e. 5 μs $\leqslant$ Time $\leqslant$ 7 μs) as shown in figures 4(a) and (b)). It is noteworthy that in figure 10 we observe the existence of a source inductance (i.e. negative value of C_1) as well. The origin of this dynamic source capacitance and inductance might be understood by the transient charge distribution on the internal circuit element of the high voltage pulse generator. When the external circuit experiences very fast voltage and current fluctuations, they induce a charge redistribution in these elements. However, such redistribution of electrical charges may not take place instantaneously. That is, the transient behaviours of capacitors (and inductors) can be different from their low-frequency behaviours. The delay time in charge redistribution under very fast voltage and current fluctuations (as is the case in our operating condition) might cause the dynamic behaviour of the parasitic capacitance which is different from its measured DC value prior to circuit connection. The detailed investigation of this phenomenon in our experiments is beyond the scope of this article and can be a subject of future study.
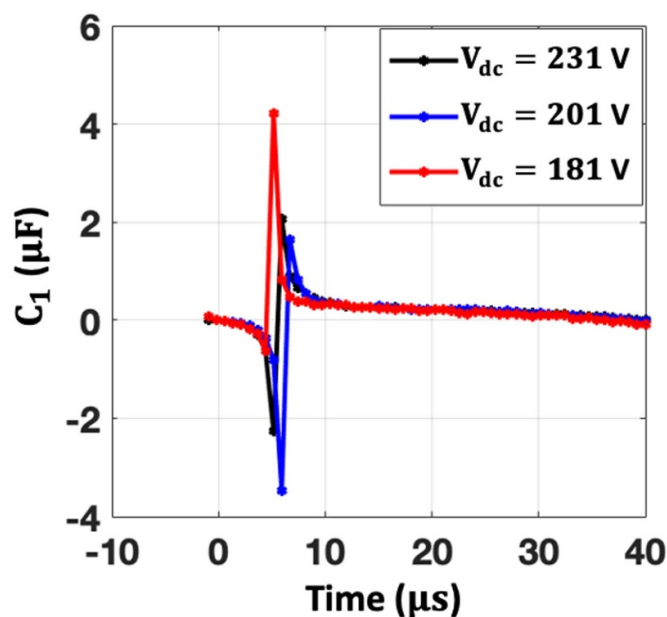
J. Phys. D: Appl. Phys. **56** (2023) 505204

A Iqbal *et al*

Figure 10. C_1 vs time estimated from equation (B1) using the measured values of $I(t)$ and $V(t)$ from figures 4(a), (b).

ORCID iDs

Asif Iqbal ⓘ https://orcid.org/0000-0001-7460-3339
Brian Z Bentz ⓘ https://orcid.org/0000-0003-1911-0018
Yang Zhou ⓘ https://orcid.org/0000-0001-6972-4822
Peng Zhang ⓘ https://orcid.org/0000-0003-0606-6855

References

[1] Kumar A, Škoro N, Gernjak W and Puač N 2021 Cold atmospheric plasma technology for removal of organic micropollutants from wastewater—a review *Eur. Phys. J.* D **75** 283

[2] Šimek M and Homola T 2021 Plasma-assisted agriculture: history, presence, and prospects—a review *Eur. Phys. J.* D **75** 210

[3] Goebel D M, Becatti G, Mikellides I G and Lopez Ortega A 2021 Plasma hollow cathodes *J. Appl. Phys.* **130** 050902

[4] He S, Li J, Qiao Y, Zhao J, Li Q and Dong L 2022 Influence of equivalent resistance on the simulation of self-pulsing discharge by using a circuit model *Eur. Phys. J.* D **76** 99

[5] Stryczewska H D and Boiko O 2022 Applications of plasma produced with electrical discharges in gases for agriculture and biomedicine *Appl. Sci.* **12** 4405

[6] Capitelli M, Casavola A, Colonna G and De Giacomo A 2004 Laser-induced plasma expansion: theoretical and experimental aspects *Spectrochim. Acta* B **59** 271

[7] Rusak D A, Castle B C, Smith B W and Winefordner J D 1998 Recent trends and the future of laser-induced plasma spectroscopy *TrAC Trends Anal. Chem.* **17** 453

[8] Vadillo J M and Laserna J J 2004 Laser-induced plasma spectrometry: truly a surface analytical tool *Spectrochim. Acta* B **59** 147

[9] Laroussi M 2018 Plasma medicine: a brief introduction *Plasma* **1** 47–60

[10] Laroussi M *et al* 2022 Low-temperature plasma for biology, hygiene, and medicine: perspective and roadmap *IEEE Trans. Radiat. Plasma Med. Sci.* **6** 127

[11] Iqbal A, Wozniak D, Rahman M Z, Banerjee S, Verboncoeur J, Zhang P and Jiang C 2022 Influence of discharge polarity on streamer breakdown criterion of ambient air in a non-uniform electric field *J. Phys. D: Appl. Phys.* **56** 035204

[12] Fu Y, Zhang P, Verboncoeur J P and Wang X 2020 Electrical breakdown from macro to micro/nano scales: a tutorial and a review of the state of the art *Plasma Res. Express* **2** 013001

[13] Iqbal A, Wen D-Q, Verboncoeur J P and Zhang P 2023 Recent advances in multipactor physics and mitigation *High Volt.* accepted (https://doi.org/10.1049/hve2.12335)

[14] Raizer Y P 1991 *Gas Discharge Physics* (Springer)

[15] Townsend J S 1925 Motion of electrons in gases *J. Franklin Inst.* **200** 563

[16] Druyvesteyn M J and Penning F M 1940 The mechanism of electrical discharges in gases of low pressure *Rev. Mod. Phys.* **12** 87

[17] Ligenza J R 1965 Silicon oxidation in an oxygen plasma excited by microwaves *J. Appl. Phys.* **36** 2703

[18] Eckbreth A C and Davis J W 1972 Rf augmentation in CO_2 closed-cycle DC electric-discharge convection lasers *Appl. Phys. Lett.* **21** 25

[19] Flamm D L, Donnelly V M and Ibbotson D E 1983 Basic chemistry and mechanisms of plasma etching *J. Vac. Sci. Technol.* B **1** 23–30

[20] Kobayashi K, Mutsukura N and Machi Y 1986 Deposition of hard carbon films by RF glow discharge method *J. Appl. Phys.* **59** 910

[21] Moreau W M 1988 *Semiconductor Lithography: Principles, Practices, and Materials* (Plenum Press)

[22] Wen D-Q, Zhang P, Krek J, Fu Y and Verboncoeur J P 2022 Higher harmonics in multipactor induced plasma ionization breakdown near a dielectric surface *Phys. Rev. Lett.* **129** 045001

[23] Iqbal A, Wong P Y, Wen D-Q, Lin S, Verboncoeur J and Zhang P 2020 Time-dependent physics of single-surface multipactor discharge with two carrier frequencies *Phys. Rev.* E **102** 043201

[24] Mirmozafari M, Iqbal A, Zhang P, Behdad N, Booske J H and Verboncoeur J P 2022 Secondary electron yield characterization of high porosity surfaces for

J. Phys. D: Appl. Phys. **56** (2023) 505204

A Iqbal *et al*

multiplactor-free microwave components *Phys. Plasmas* **29** 082109

[25] Zhang P, Valfells Á, Ang L K, Luginsland J W and Lau Y Y 2017 100 Years of the physics of diodes *Appl. Phys. Rev.* **4** 011304

[26] Zhang P, Ang Y S, Garner A L, Valfells Á, Luginsland J W and Ang L K 2021 Space–charge limited current in nanodiodes: ballistic, collisional, and dynamical effects *J. Appl. Phys.* **129** 100902

[27] Benford J, Swegle J A and Schamiloglu E 2015 *High Power Microwaves* 3rd edn (Taylor & Francis)

[28] Mieno T 2016 *Plasma Science and Technology: Progress in Physical States and Chemical Reactions* (InTech)

[29] Phelps A V and Petrovic Z L 1999 Cold-cathode discharges and breakdown in argon: surface and gas phase production of secondary electrons *Plasma Sources Sci. Technol.* **8** R21

[30] Zhou Y and Zhang P 2021 Quantum efficiency of photoemission from biased metal surfaces with laser wavelengths from UV to NIR *J. Appl. Phys.* **130** 064902

[31] Jensen K L 2018 *Introduction to the Physics of Electron Emission* (Wiley)

[32] Fowler R H 1931 The analysis of photoelectric sensitivity curves for clean metals at various temperatures *Phys. Rev.* **38** 45

[33] DuBridge L A 1932 A further experimental test of Fowler's theory of photoelectric emission *Phys. Rev.* **39** 108

[34] DuBridge L A 1933 Theory of the energy distribution of photoelectrons *Phys. Rev.* **43** 727

[35] Bechtel J H, Smith W L and Bloembergen N 1975 Four-photon photoemission from tungsten *Opt. Commun.* **13** 56

[36] Spicer W E 1958 Photoemissive, photoconductive, and optical absorption studies of alkali-antimony compounds *Phys. Rev.* **112** 114

[37] Berglund C N and Spicer W E 1964 Photoemission studies of copper and silver: theory *Phys. Rev.* **136** A1030

[38] Krolikowski W F and Spicer W E 1969 Photoemission studies of the noble metals I. Copper *Phys. Rev.* **185** 882

[39] Krolikowski W F and Spicer W E 1970 Photoemission studies of the noble metals II. Gold *Phys. Rev. B* **1** 478

[40] Zhou Y and Zhang P 2020 A quantum model for photoemission from metal surfaces and its comparison with the three-step model and Fowler–DuBridge model *J. Appl. Phys.* **127** 164903

[41] Zhang P and Lau Y Y 2016 Ultrafast strong-field photoelectron emission from biased metal surfaces: exact solution to time-dependent Schrödinger equation *Sci. Rep.* **6** 19894

[42] Luo Y and Zhang P 2021 Ultrafast optical-field-induced photoelectron emission in a vacuum nanoscale gap: an exact analytical formulation *Appl. Phys. Lett.* **119** 194101

[43] Luo Y and Zhang P 2018 Ultrafast strong-field photoelectron emission due to two-color laser fields *Phys. Rev. B* **98** 165442

[44] Luo Y and Zhang P 2019 Analysis of two-color laser-induced electron emission from a biased metal surface using an exact quantum mechanical solution *Phys. Rev. Appl.* **12** 044056

[45] Luo Y, Zhou Y and Zhang P 2021 Few-cycle optical-field-induced photoemission from biased surfaces: an exact quantum theory *Phys. Rev. B* **103** 085410

[46] Zhou Y and Zhang P 2022 Unraveling quantum pathways interference in two-color coherent control of photoemission with bias voltages *Phys. Rev. B* **106** 085402

[47] Morgan F, Evans L R and Morgan C G 1971 Laser beam induced breakdown in helium and argon *J. Phys. D: Appl. Phys.* **4** 225

[48] Zhang S, Wang X, He M, Jiang Y, Zhang B, Hang W and Huang B 2014 Laser-induced plasma temperature *Spectrochim. Acta* B **97** 13

[49] Petrović Z L and Phelps A V 1993 Oscillations of low-current electrical discharges between parallel-plane electrodes I. Dc discharges *Phys. Rev. E* **47** 2806

[50] Phelps A V, Petrović Z L and Jelenković B M 1993 Oscillations of low-current electrical discharges between parallel-plane electrodes III. Models *Phys. Rev. E* **47** 2825

[51] Jelenković B M, Rózsa K and Phelps A V 1993 Oscillations of low-current electrical discharges between Parallel-plane electrodes. II. Pulsed discharges in H_2 *Phys. Rev. E* **47** 2816

[52] Horváth B, Derzsi A, Schulze J, Korolov I, Hartmann P and Donkó Z 2020 Experimental and kinetic simulation study of electron power absorption mode transitions in capacitive radiofrequency discharges in neon *Plasma Sources Sci. Technol.* **29** 055002

[53] Petrović Z L and Phelps A V 1997 Temporal and constriction behavior of low-pressure, cathode-dominated argon discharges *Phys. Rev. E* **56** 5920

[54] Hagstrum H D 1953 Electron ejection from Mo by He^+, He^{++}, and He_2^+ *Phys. Rev.* **89** 244

[55] Rogowski W 1929 Stoßspannung und Durchschlag bei Gasen *Arbeiten aus dem Elektrotechnischen Institut der Technischen Hochschule Aachen: Band III: 1928* ed W Rogowski (Springer) pp 57–64

[56] Rogowski W and Wallraff A 1938 Zündung und Zündspannungsänderung *Z. Phys.* **108** 1–18

[57] Fu Y, Krek J, Zhang P and Verboncoeur J P 2018 Evaluating microgap breakdown mode transition with electric field non-uniformity *Plasma Sources Sci. Technol.* **27** 095014

[58] Go D B and Pohlman D A 2010 A mathematical model of the modified Paschen's curve for breakdown in microscale gaps *J. Appl. Phys.* **107** 103303

[59] Venkattraman A and Alexeenko A A 2012 Scaling law for direct current field emission-driven microscale gas breakdown *Phys. Plasmas* **19** 123515

[60] Ramo S 1939 Currents induced by electron motion *Proc. IRE* **27** 584

[61] Shockley W 2004 Currents to conductors induced by a moving point charge *J. Appl. Phys.* **9** 635

[62] Boeuf J P and Marode E 1982 A Monte Carlo analysis of an electron swarm in a nonuniform field: the cathode region of a glow discharge in helium *J. Phys. D: Appl. Phys.* **15** 2169

[63] Dexter A C, Farrell T and Lees I M 1989 Electronic and ionic processes and ionic bombardment of the cathode in a DC hydrogen glow discharge *J. Phys. D: Appl. Phys.* **22** 413

[64] Sommerer T J, Hitchon W N G and Lawler J E 1989 Self-consistent kinetic model of the cathode fall of a glow discharge *Phys. Rev. A* **39** 6356

[65] Fierro A, Moore C, Scheiner B, Yee B T and Hopkins M M 2017 Radiation transport in kinetic simulations and the influence of photoemission on electron current in self-sustaining discharges *J. Phys. D: Appl. Phys.* **50** 065202